International Journal of Nanomedicine

Dovepress

open access to scientific and medical research

Open Access Full Text Article

ORIGINAL RESEARCH

Application of Three-Dimension Printing Nano-Carbonated-Hydroxylapatite to the Repair of Defects in Rabbit Bone

Shujie Wang[1,2], Chunyan Shao[2], Xingkai Zhao[1], Yizhe Guo[1], Houhui Song[2], Lida Shen[3], Zhenlei Zhou[1], Zhen Li[4,5]

[1]College of Veterinary Medicine, Nanjing Agricultural University, Nanjing, Jiangsu, 210095, People's Republic of China; [2]College of Animal Science and Technology & College of Veterinary Medicine, Zhejiang Agriculture and Forestry University, Hangzhou, Zhejiang, 311300, People's Republic of China; [3]College of Mechanical and Electrical Engineering, Nanjing University of Aeronautics and Astronautics, Nanjing, Jiangsu, 210016, People's Republic of China; [4]College of Resources and Environmental Sciences, Nanjing Agricultural University, Nanjing, Jiangsu, 210095, People's Republic of China; [5]State Key Laboratory of Palaeobiology and Stratigraphy, Nanjing Institute of Geology and Palaeontology and Center for Excellence in Life and Paleoenvironment, Chinese Academy of Sciences, Nanjing, Jiangsu, 210008, People's Republic of China

Correspondence: Zhenlei Zhou, College of Veterinary Medicine, Nanjing Agricultural University, Nanjing, Jiangsu, 210095, People's Republic of China, Tel +86 (25) 84395505, Email zhouzl@njau.edu.cn; Zhen Li, College of Resources and Environmental Sciences, Nanjing Agricultural University, Nanjing, Jiangsu, 210095, People's Republic of China, Tel/Fax +86 (25) 84399827, Email lizhen@njau.edu.cn

Introduction: Hydroxylapatite (HAp) is a biodegradable bone graft material with high biocompatibility. However, the clinical application of HAp has been limited due to the poor absorption rate in vivo.

Methods: In this study, carbonated hydroxylapatite (CHAp) with a chemical composition similar to natural bone was synthesized. HAp and CHAp scaffolds were fabricated by 3D printing. Each material was designed by two types of scaffold model with a maximum width of 8 mm and a thickness of 2 mm, ie, structure I (round shape) and structure II (grid shape). Then, the HAp scaffolds were loaded with lutein. These scaffolds were implanted into the 8 mm bone defect on the top of the rabbit skull within 3 hours in the morning. The curative effects of the scaffolds were assessed two months after implantation.

Results: The 3D printed scaffolds did not cause severe inflammation or rejection after implantation. It showed that the porous structures allow bone cells to enter into the scaffolds. Furthermore, CHAp scaffolds were more biocompatible than HAp scaffolds, and showed a higher level of degradation and new bone formation after implantation. Structure II scaffolds with a smaller mineral content degraded faster than structure I, while structure I had better osteoconductive properties than structure II. Besides, the addition of lutein significantly enhanced the rate of new bone formation.

Discussion: The uniqueness of this study lies in the synthesis of 3D printed CHAp scaffolds and the implantation of CHAp in rabbit bone defects. The incorporation of suitable carbonate and lutein into HAp can enhance the osteoinductivity of the graft, and CHAp has a faster degradation rate in vivo, all of which provide a new reference for the research and application of apatite-based composites.

Keywords: bone, 3D printing, hydroxylapatite, lutein, repair

Introduction

The bone defect caused by severe trauma, infection, tumor resection, etc. requires bone grafting for better recovery.[1,2] It is estimated that over 2.2 million orthopedic procedures involving bone grafting are performed worldwide annually.[3] Both autologous and allogeneic bone grafts offer significant advantages in osteo-regeneration.[4–7] However, secondary bone damage, complications, or immune rejection might limit the clinical use of graft materials.[8–10]

The emergence of synthetic bone substitutes offers more options for bone grafting, and ceramic-based bone substitutes account for about 60% of the synthetic graft market.[11] Hydroxylapatite (HAp) has a similar chemical composition analogous to natural bone minerals.[12,13] It has excellent biocompatibility, osteoconductivity, and osteoinductivity in bone regeneration.[14–16] However, the relatively high Ca/P ratio and crystallinity of HAp delay the resorption

Received: 15 October 2023
Accepted: 13 February 2024
Published: 20 February 2024

rate in vivo.[17] The bone mineral is a variety of HAp, ie, carbonated-hydroxylapatite (CHAp), with the incorporation of 4–8 wt.% carbonate.[18] CHAp is able to promote initial bone regeneration during the repair of bone defects.[14,19] In addition, CHAp shows high dissolution capability in body physiological environment (pH 7.4).[20] A previous study has reported faster degradation of CHAp in a rat shin defect compared to other calcium phosphate ceramic materials, including HAp, β-tricalcium phosphate, and silicon-containing HAp.[21]

Although CHAp can be regarded as bone apatite, the direct use of CHAp powder as a bone substitute would induce an inflammatory response upon implantation.[20] The first pathway of enhancement is structural modification. Three-dimensional (3D) printing technology can process ceramic powder into porous scaffolds. Microporosity improves bone growth into scaffolds by increasing the surface area for protein sorption and providing attachment for osteoblasts.[22,23] Moreover, the 3D printed scaffold is suitable as a drug carrier due to the interconnected pores.[20]

In addition to the physical structure, biological or biochemical components are also critical for bone repair in clinical practice. Carotenoids are natural antioxidants that are metabolized in various chemical entities with multifarious properties in the human body, including scavenging free radicals along with the provision of vitamin A activity. Globally, the demand for carotenoids increased from 1.5 billion dollars (2014) to 1.8 billion dollars (2019) due to their potent health-modulating properties.[24,25] Increased ingestion of carotenoids particularly β-cryptoxanthin, and lutein/zeaxanthin are linked with a decreased potential of osteoporotic fractures in the elderly.[26,27] It was shown that β-cryptoxanthin increased calcium and phosphorus deposition by osteoblasts and promoted protein synthesis in bone.[28] Lutein and lycopene have also been shown to promote osteogenesis.[29–32] In addition, carotenoids may play an important role in bone repair. It has been suggested that the integration/ingrowth capabilities of spongy femoral and tibial bones following total knee joint replacement correlate with the carotenoid content of the bone and surrounding fatty tissue.[33] Combining antioxidants with graft materials may therefore help bone regeneration.

The novelty of this study lies in the fabrication of 3D printed CHAp scaffolds and the application of CHAp in the treatment of bone defects. In this study, CHAp with a chemical composition similar to natural bone was synthesized. The biocompatibility and degradation rate of CHAp are superior to those of HAp. Due to the fact that nano-CHAp powders cannot be directly applied to bone grafts, the effectiveness of CHAp in bone defects has rarely been reported. Therefore, porous CHAp scaffolds were fabricated by digital light processing and a light-curing printer in this study. In addition, the curative effects of HAp scaffolds, CHAp scaffolds and lutein were evaluated in rabbit calvarial defects with a view to informing the clinical application of CHAp.

Materials and Methods

Synthesize CHAp

CHAp powder (Type B) was prepared based on the previously proposed protocol.[34]

2.5 L of ultrapure water was heated to 60 °C in the reactor on a magnetic stirrer. Subsequently, 9.45 g of $NaHCO_3$ (Acros-Organics, 99.5%), 250 mL 0.15 M $Ca(NO_3)_2{\bullet}4H_2O$ (Sigma-Aldrich, 99%), and 250 mL 0.09 M NaH_2PO_4 (Sigma-Aldrich, 98%) solution were added into the reactor bath. During the synthesis of CHAp, the pH was adjusted to 9.0 ± 0.5 and maintained by adding 0.5 M NaOH (Acros-Organics, 97%). The precipitates were washed three times with ultrapure water and then were dried in a vacuum freeze dryer for 24 h and ground to 5 μm powder for 3D printing.

3D Printing

The HAp and CHAp powders are mixed with the photosensitive resin (Shanghai Guangyi Chemical Co., Ltd., China) at a mass ratio of 3:1 respectively, and a dispersant (sodium polyacrylate, Hebei Jinhong Chemical Co., Ltd., China) of 3% by weight is added. The mixed slurry is well stirred in a vacuum mixer for 1 h. The porous three-dimensional bone scaffold model was designed according to the previous research.[35] The model data were imported into a digital light processing and light-curing printer developed by Nanjing University of Aeronautics and Astronautics.[36] The thickness of each printing layer used for printing composite ceramic slurry was 0.02 mm. After printing, the green body of the scaffold was washed in absolute ethanol for 5 min via ultrasound to remove the extra slurry on the surface, and the extra slurry in the hole was eventually removed via air gun. After the green body was dried, it was put in a tube furnace for

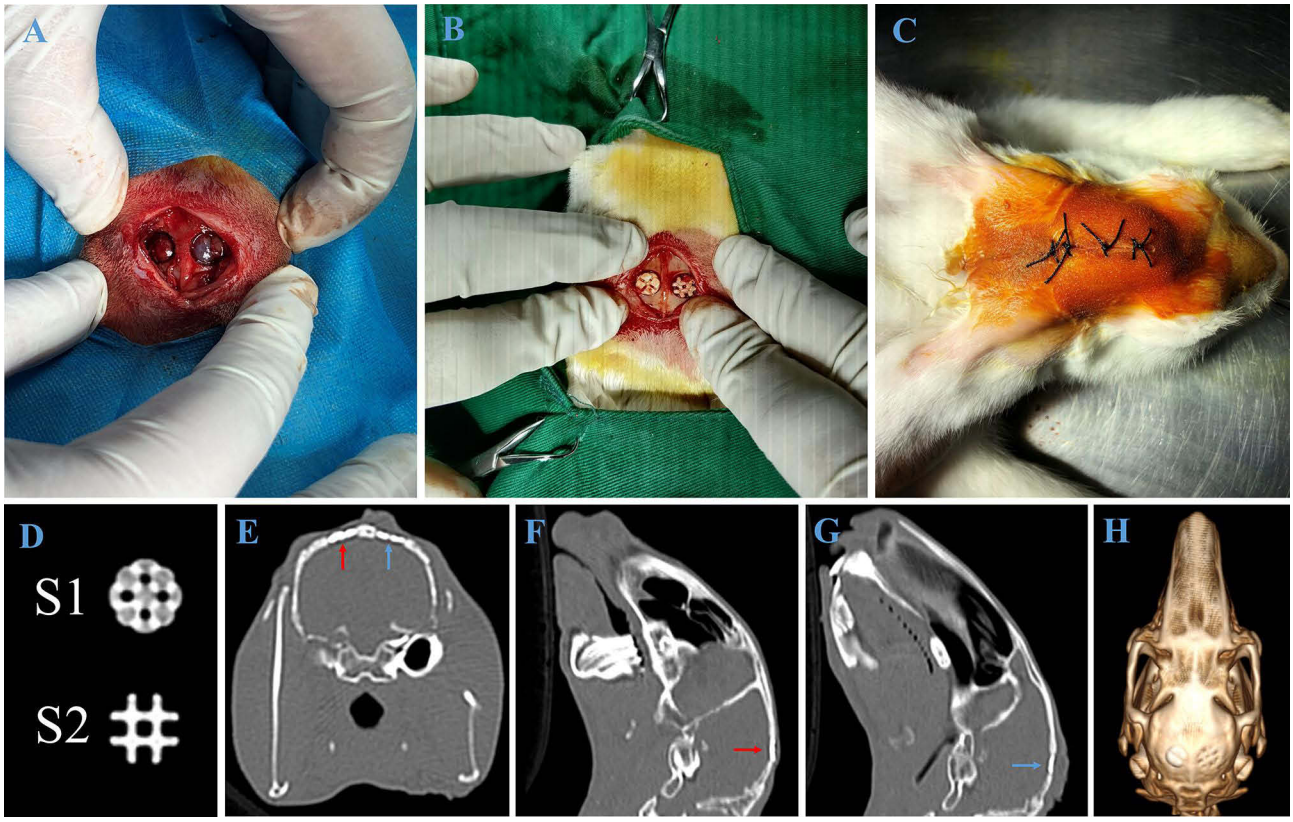

Figure 1 Scaffolds implantation and CT examination. (**A**–**C**) Surgical implantation of scaffolds in the rabbit. (**D**) Radiographs of the two structural scaffolds. (**E**) Transverse view of CT, red arrow points to the S1 scaffold, blue arrow points to the S2 scaffold. (**F** and **G**) Sagittal view of CT, red arrow points to the S1 scaffold, blue arrow points to the S2 scaffold. (**H**) CT 3D reconstruction image.

heat treatment at 500 °C for 4 h. The organic materials in the body, such as resin, were removed. Finally, the green body was sintered at 600 °C for 1.5 h to obtain a porous scaffold. Two types of scaffold models were designed (see Figure S1). Structure I (S1) has a round shape and structure II (S2) has a grid shape with less mineral content (see Figure 1). All scaffolds have a maximum width of 8 mm and a thickness of 2 mm. The scaffolds used in this study have been ultrasonically cleaned and autoclave sterilization (121.3°C for 30 min).

Scaffold Characteristics

The density and mineral content of the scaffolds were measured by a dual-energy X-ray absorption measuring instrument (InAlyzer, Medikors, Inc., Gyeonggi-do, Korea). The acquired images were analyzed by using the InAlyzer 1.0 image processing system.

The porosity of the scaffolds was tested by the boiling method. The dry weight of the scaffolds were recorded as m_0. The scaffolds were boiled in distilled water for 2 h. After cooling, the floating weight of scaffolds were detected and recorded as m_1. Then, the wet scaffolds were weighed and recorded as m_2. The porosity of the scaffolds was calculated by the formula: $P = (m_2 - m_0)/(m_2 - m_1)$.

The chemical composition of the scaffolds was measured by Fourier transform infrared (Nicolet iS5, Thermo Fisher Scientific, Inc., USA) and Raman imaging microscope (DXR2xi, Thermo Fisher Scientific, Inc., USA). The spectral region of 500–2500 cm^{-1} was recorded using a 532 nm laser in the detection of Raman spectroscopy. The laser power was set to 8.0 Mw, and each point performed 200×0.01 s scans. The point spacing of Raman mapping measurements was 2 μm.

The surface morphology of the scaffolds was measured by scanning electron microscopy (Regulus8100, Hitachi, Ltd., Japan).

Biocompatibility Assessment of the 3D Printed Scaffolds

The mouse osteoblast precursor cell line (MC3T3-E1 Subclone 14, purchased from Mingzhou Biotechnology Co., LTD, Ningbo, China) was used in this study. The in-vitro cell culture experiments were repeated three times, with three replications in each group.

MC3T3 cells were cultured in glucose Dulbecco's modified eagle medium (DMEM containing 10% fetal bovine serum and 1% penicillin-streptomycin, Gibco, USA) at 37 °C under a 5% CO_2 atmosphere.

The scaffolds were submerged in a 100 mL DMEM medium and incubated in a shaker (3 Hz, 37°C) for 24 h. The solution was centrifuged and the supernatant was taken as the extraction liquid of scaffolds. MC3T3 cells were cultured in the extraction liquid for 1, 2, and 3 days, and cell viability was detected by Cell Counting Kit-8 (CCK-8).

The scaffolds were placed in the 48-well plate and inoculated with 10^4 MC3T3 cells per well. After 12 h of incubation, the scaffold was removed from the medium and placed in a new 48-well plate. The adherent cells were digested with trypsin and then counted using a hemocytometer. Cell viability was measured by CCK-8 after 1, 3, and 7 days of culture.

The Osteogenic Function of MC3T3 Cells

The scaffolds were placed in the 48-well plate and inoculated with 10^4 MC3T3 cells per well. Cells were cultured in mineralization induction DMEM (vitamin C 50 μg/mL, β-Glycerophosphate Disodium 10 mM). After 14 days of incubation, cells on the scaffolds were lysed using RIPA buffer. Then, a BCA protein assay kit and an alkaline phosphatase (ALP) kit were used to measure the ALP activity.

MC3T3 cells were treated with lutein at 0.1, 1, and 10 μM for 24h, then total RNA and protein were extracted. The expression of osteogenic-related genes was detected by Real-time quantitative polymerase chain reaction (RT-qPCR) (Applied Biosystems, Inc., Foster City, CA, USA).

MC3T3 cells were inoculated in 6 cm cell culture dishes at a density of 5×10^4 cells/mL. The experiment was divided into three groups and incubated for 21 d using mineralization induction medium with lutein concentrations of 0, 1 μM and 10 μM, respectively. The samples were fixed in 4% paraformaldehyde for 15 min, washed three times with ultrapure water, and then stained with 0.1% alizarin red staining solution for 30 min.

Evaluation of 3D Printed Scaffolds

Twenty-four 4-month-old male New Zealand white rabbits (Qinglong Mount Hen Company, Nanjing, China), with an average initial weight of ~2.2 kg were used in this experiment. They were randomly divided into blank, HAp, lutein, and CHAp four groups (6 rabbits in each group) after a week of pre-feeding. All rabbits were raised in single cages in a room with environmental control (temperature: 20 ± 5°C, relative humidity: 50 ± 10%). The rabbits had free access to water and were fed commercial feed based on body weight.

Rabbits were anesthetized with 1% propofol (1 mg/kg·min, intravenous injection). A 3 cm long skin incision over the linea media was made, and the tissue was dissected to adequately expose the calvaria. Using an electric handpiece with a trephine bur, two circular bicortical defects (8 mm in diameter) were created symmetrically to the midline of the calvaria in the parietal bones under constant saline irrigation. The defect was left empty in the blank group (Figure 1A). HAp, lutein, and CHAp groups were implanted with HAp scaffolds, lutein-treated HAp scaffolds, and CHAp scaffolds respectively, with S1 scaffold on the left bone defect and S2 scaffold on the right (Figure 1B). Then the periosteum and skin were sutured to close the surgical access (Figure 1C). Radiograph of the two structural scaffolds is shown in Figure 1D. Scaffolds in the lutein group were soaked in 10 μM sterile lutein solution for 24 h and lyophilized by a vacuum freeze dryer, and then coated with a sodium hyaluronate gel containing 10 μM lutein. Scaffolds in the HAp and CHAp groups were coated with hyaluronidase gel without lutein. 24 rabbits were divided into four groups for surgeries simultaneously, and all rabbits were finished implantation within three hours in the morning.

Rabbits were given Baytril (0.3 mL/kg) to prevent inflammation and meloxicam (0.1 mL/kg) to reduce postoperative pain for 2 d. Blood was collected from the ear vein for blood routine examination at 1, 4, and 7 d after the operation, and a head CT was performed on the second day after the operation (Figure 1E–H).

The rabbits were sacrificed on the 60th day after the operation, and their calvaria was collected and preserved in 4% paraformaldehyde. Micro-CT (Xradia 520Versa, Zeiss, Inc., Germany) was performed to quantify the volume of bone formation and residual scaffold within the defects. Raman imaging microscope was used to measure the chemical composition of newly regenerated bone. Then, the calvaria samples were embedded in paraffin blocks after decalcification for routine sectioning and staining with Hematoxylin-eosin (HE) and Safranin O-fast green (SF). Recovery of bone defects in the blank group was assessed by CT and dual-energy X-ray absorption measuring instruments.

Statistical Analyses

All the data were analyzed using IBM SPSS Statistics 21 (IBM Corp., Armonk, NY, USA). The differences among the groups were determined by one-way analysis of variance (ANOVA, Turkey, and Dunnet's T3). The data are presented as the mean ± standard deviation. Significant differences were accepted if $P < 0.05$.

Ethics Committee Approval

All animal experiments were performed in accordance with the Institute of Laboratory Animal Resources guidelines. Ethical approval was granted by the Institutional Animal Care and Use Committee of Nanjing Agricultural University (NJAU.NO20210706112).

Results

Density, Porosity and Chemical Composition of 3D Printed Scaffolds

The results of dual-energy X-ray absorption measuring instrument showed (see Table 1) that the mineral content and density of the HAp and CHAp scaffolds were relatively similar. The mineral content of S1 scaffolds (0.84 g) was significantly greater than that of S2 scaffolds (0.58 g). The HAp and CHAp scaffolds have similar porosities, ranging from 27.2% to 30.9% (see Table 1).

In Figure 2, the most intense peak was the ν1 P-O symmetric stretch located at 1017 cm^{-1}, which confirmed the phosphate phase in HAp and CHAp scaffolds.[37] The bands observed at 871 and 1413 cm^{-1} are characteristic peaks for carbonates, confirming the dominant presence of type B carbonation in CHAp scaffolds.[38] The chemical composition of 3D printed scaffolds was further verified by Raman imaging results (see Figure 2). The correlation between the Raman imaging ranges of both the HAp and CHAp scaffolds was above 90%, indicating a relatively homogeneous composition. The distinct carbonate characteristic peak located at 1070 cm^{-1} in the spectrum of CHAp scaffold proved the existence of carbonate.

The Surface Morphology of 3D Printed Scaffolds

The surface morphology of bone grafts has an important influence on cell adhesion, proliferation, and new bone formation. The SEM imaging (see Figure 3) showed that there are significant differences in the morphology of the HAp and CHAp scaffolds. Compared to the HAp scaffold, the CHAp scaffold had larger surface aggregated particles and larger inter-particle pores. In addition, there were many irregular protrusions on the aggregated particles of the CHAp scaffold, which might suggest a looser microstructure.

Table 1 Density and Porosity Level of 3D Printed Scaffolds (n=6)

Group	Mineral Content (g)	Density (g/cm^3)	Porosity Level (%)
HAp S1	0.082±0.001	0.278±0.004	27.2±0.9
HAp S2	0.057±0.001	0.254±0.003	28.5±1.2
CHAp S1	0.084±0.001	0.279±0.003	29.8±1.2
CHAp S2	0.058±0.001	0.266±0.005	30.9±1.1

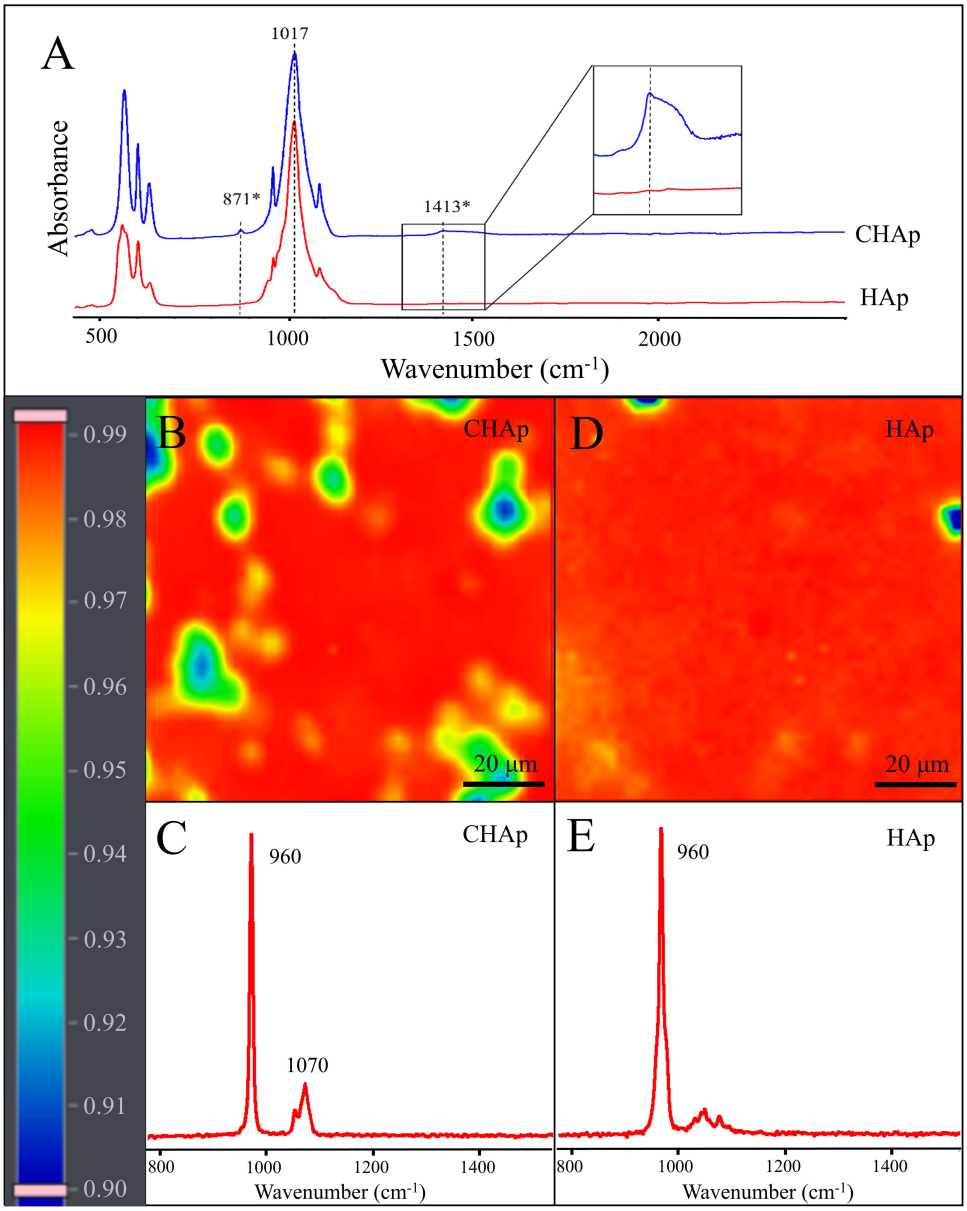

Figure 2 Chemical composition analysis of 3D printed scaffolds. (**A**) The infrared spectrum of the HAp and CHAp scaffolds. (**B** and **D**) Distribution maps of CHAp and HAp scaffolds, the color of the scanning area represents the correlation with the representative Raman spectra. (**C** and **E**) Representative Raman spectra of CHAp and HAp scaffolds.

Biocompatibility of the 3D Printed Scaffolds

There was no significant difference in the cell viability of MC3T3 cells after 1, 2, and 3 d of culture in the extracts of HAp and CHAp scaffolds (see Figure 4A), indicating that the 3D printed scaffolds had no significant cytotoxicity.

The cell count results (see Figure 4B) showed that the CHAp scaffold had a significantly higher number of cell attachments within 12 h than the HAp scaffold, which suggested that the CHAp scaffold had better cell adhesion properties. In addition, the proliferation rate of MC3T3 cells on the CHAp scaffold was significantly greater than that on the HAp scaffold (see Figure 4C).

The Osteogenic Function of MC3T3 Cells

ALP reflects the activity of osteoblasts and the level of osteogenic differentiation. As shown in Figure 4D, after 14 d of culture, the ALP activity of MC3T3 cells on the CHAp scaffold was significantly higher than that of MC3T3 cells on the HAp scaffold, indicating that the CHAp scaffold had better osteoinductivity.

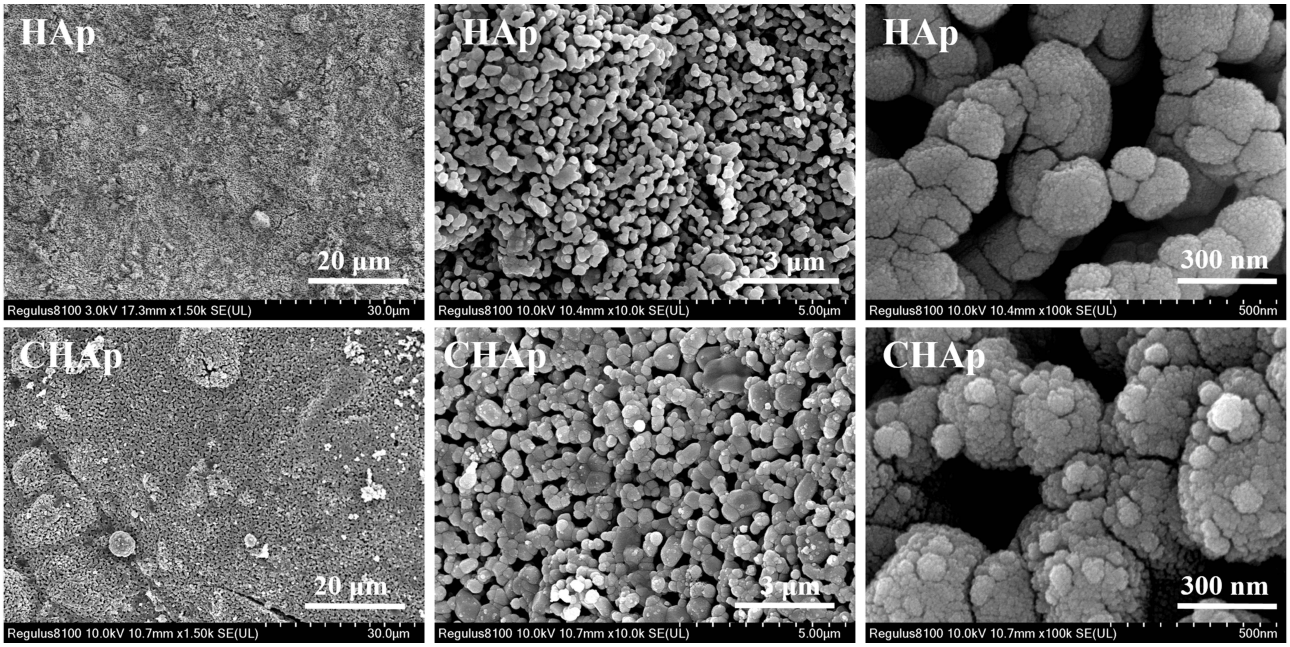

Figure 3 Morphology of HAp and CHAp scaffolds.

The RT-qPCR results (Figure 5A–C) showed that both 1 and 10 μM lutein significantly promoted the mRNA expression of ALP, RUNX2, OCN, BSP, OPN, β-catenin, and TCF4, and 10 μM lutein had a more pronounced effect.

Alizarin red reacts with calcium salts to form red calcified nodules. After 1 and 10 μM lutein treatment for 21 d, MC3T3 cells deposited a large number of calcium salts around the culture dish, while the group without lutein only had punctate red mineralized particles (Figure 5D–F). Both 1 and 10 μM lutein could promote the mineralization of osteoblasts in vitro.

Blood Routine Examination

Bone injuries typically undergo a period of hematoma and acute inflammation for about 7 d. The results of white blood cell counts (WBC) showed an increase in the number of leucocytes postoperatively (see Figure 6). The rabbits in the blank group demonstrated a more pronounced increase in leucocyte counts at 1–4 d postoperatively. In contrast, the rabbits in the lutein group showed a relatively low postoperative leucocyte count. In addition, eosinophil counts in rabbits significantly increased one day after the implantation of the scaffolds. This indicator returned to the normal levles recommended by clinical practice after day 4, indicating that the scaffolds may have caused a transient hypersensitivity reaction.

Radiological Examination of Calvarial Defects

In the blank group, the bone defect was poorly repaired, with only a small amount of new bone was formed at the edge of the defect (see Figure 7A), indicating that the 8 mm diameter bone defect in calvaria did not heal by themselves.

The HAp scaffold still maintained a relatively complete structure after 60 d of implantation in the cranial defect (see Figure 7B and C). The edge of the scaffold was covered with new bone, but the outer surface of the scaffold was rarely attached to the new bone. In addition, newly regenerated bone can grow into the scaffold along the gaps designed by 3D printing. CHAp scaffold had undergone significant resorption in vivo, particularly in S2, which was almost completely encapsulated by new bone and eroded inside, leaving the scaffold structurally incomplete (see Figure 7D). The inner surface of the S1 scaffolds in the CHAp and lutein groups was essentially completely encapsulated by new bone, whereas a large gap remained in the S2 scaffolds (Figure 7E–G), indicating that the osteoconductivity of the S1 scaffold was superior to that of the S2 scaffold.

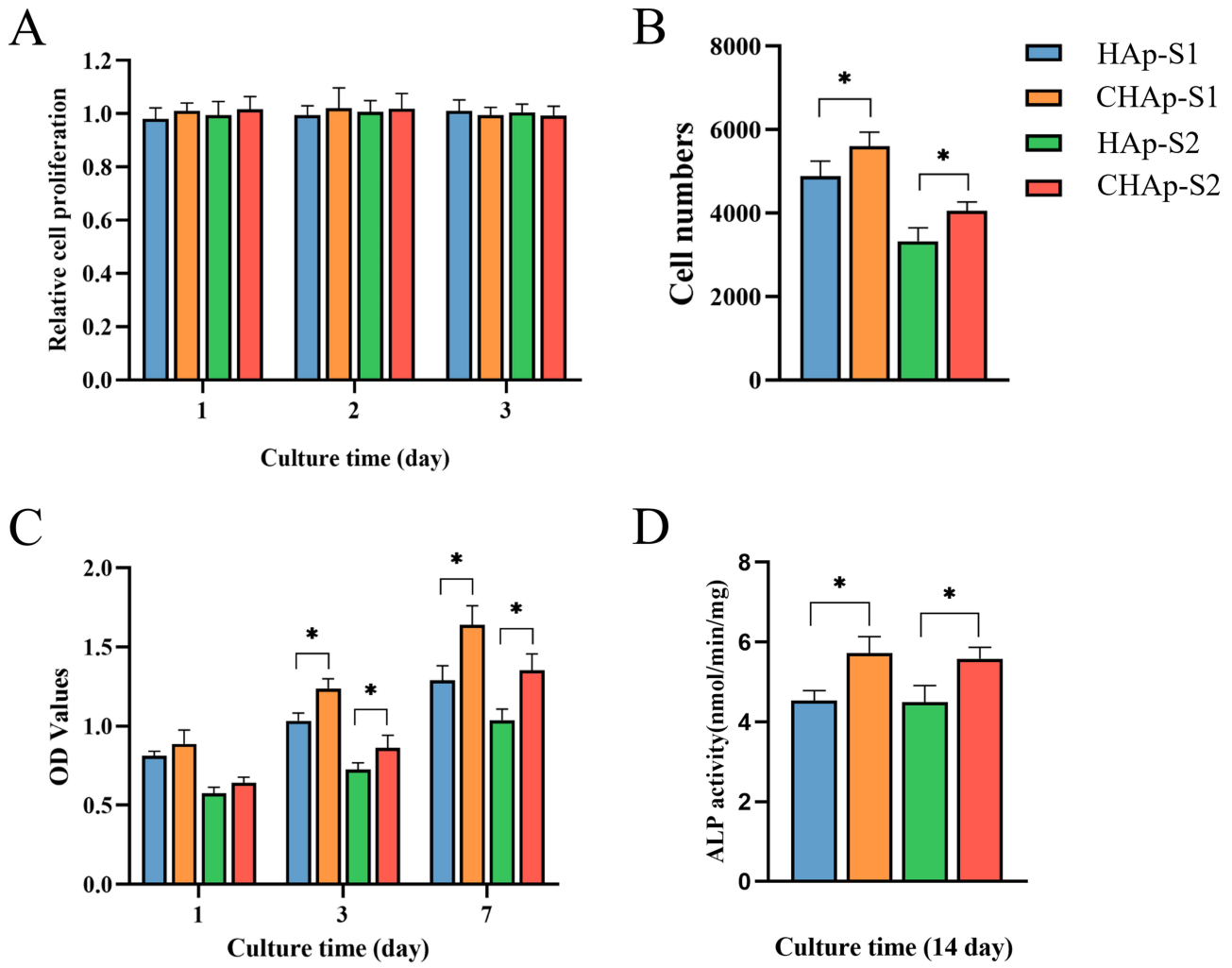

Figure 4 The cytocompatibility of HAP and CHAp scaffolds (n=3). (**A**) Cytotoxicity of the extract of HAP and CHAp scaffolds. (**B**) MC3T3 cell attachment number of HAP and CHAp scaffolds within 12 h. (**C**) The proliferation rate of MC3T3 cells on the HAP and CHAp scaffolds. (**D**) The ALP activity of MC3T3 cells on the HAP and CHAp scaffolds. *P* values were calculated along with comparisons between different groups (**P*<0.05).

The volume of new bone within the defect was significantly higher in the lutein and CHAp group than in the HAp group. The residual volume of the scaffold was smaller in the CHAp group than in the HAp and lutein groups (Figure 7H). Moreover, there was a significant increase in new bone formation and material resorption for the CHAp S2 scaffold compared to both the HAp S2 scaffold and the lutein-treated S2 scaffold. In addition, the volume ratio of the S1 and S2 scaffolds after implantation increased significantly compared to the initial volume ratio (Figure 7I), indicating that the resorption rate of the S2 scaffold was greater than that of the S1 scaffold.

Histological Observations of Calvarial Defects

Histological staining of the explanted calvarial specimens was performed to evaluate the recovery of bone defects (Figure 8). Safranin-O stained cartilage red in proportion to its proteoglycan content and fast green stained bone green. No red-stained cartilage tissue was observed in any of the bone sections, suggesting that the process of bone repair was intramembranous ossification, ie, cells differentiate directly to osteoblasts and start depositing bone matrix within a membranous tissue.

HE staining showed that the bone defect was surrounded by connective tissue. In addition, the high magnification imaging demonstrated numerous bone cells in the interior of graft scaffolds in the HAp, lutein, and CHAp groups. This

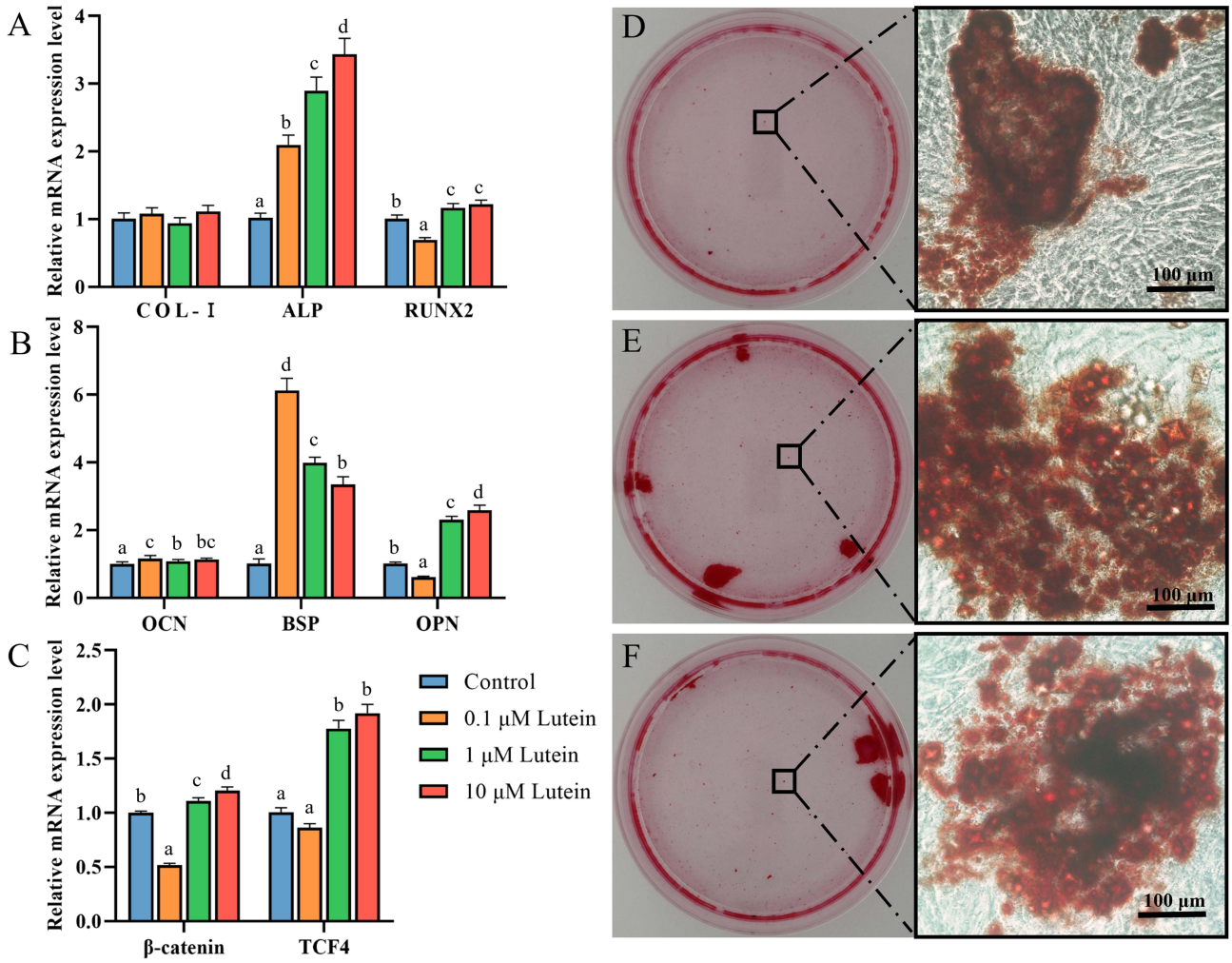

Figure 5 Lutein promotes osteogenesis of osteoblasts (n=3). (**A–C**) The expression of osteogenesis-related mRNA under different treatment conditions. Mineralization of MC3T3 cells cultured in (**D**) mineralization-induced medium, mineralization-induced medium containing (**E**) 1 μM, and (**F**) 10 μM lutein for 21 days. The red area is a deposit of calcium salts colored by alizarin red. Bars with different letters between each group indicated a significant difference at $P < 0.05$ level.

phenomenon suggested that the bone cells could grow into the scaffolds via micro-pores during the process of bone repair.

Raman Analysis on Newly Regenerated Bone Within the Defects

The 960 cm^{-1} peak with the highest intensity represents the P-O stretching vibration of PO_4^{3-}, demonstrating that the neogenic bone mineral is in the phosphate phase. 1070 cm^{-1} peak is mainly attributed to the C-O stretching vibration of CO_3^{2-}, representing the carbonate component of the neogenic bone. An envelope of peaks centered at ~2940 cm^{-1} was assigned to C-H stretching vibrations in multiple organic matters, which include collagen and non-collagenous proteins. The area ratio of the 2940 cm^{-1} peak to the 960 cm^{-1} peak allows an assessment of the amount of mineral deposition in new bone. In addition, the full width at half maximum (FWHM) of the 960 cm^{-1} peak can be used to assess the crystallinity of the bone mineral, the larger the FWHM, the lower the crystallinity.

As shown in Figure 9, the 2940 /960 cm^{-1} peak area ratio of new bone in the lutein and CHAp groups was smaller than that of the HAp group, which demonstrated that both lutein and CHAp scaffold enhanced bone mineral deposition and promoted bone maturation. Furthermore, the larger FWHM in the new bone of the HAp group suggested lower bone mineral crystallinity.

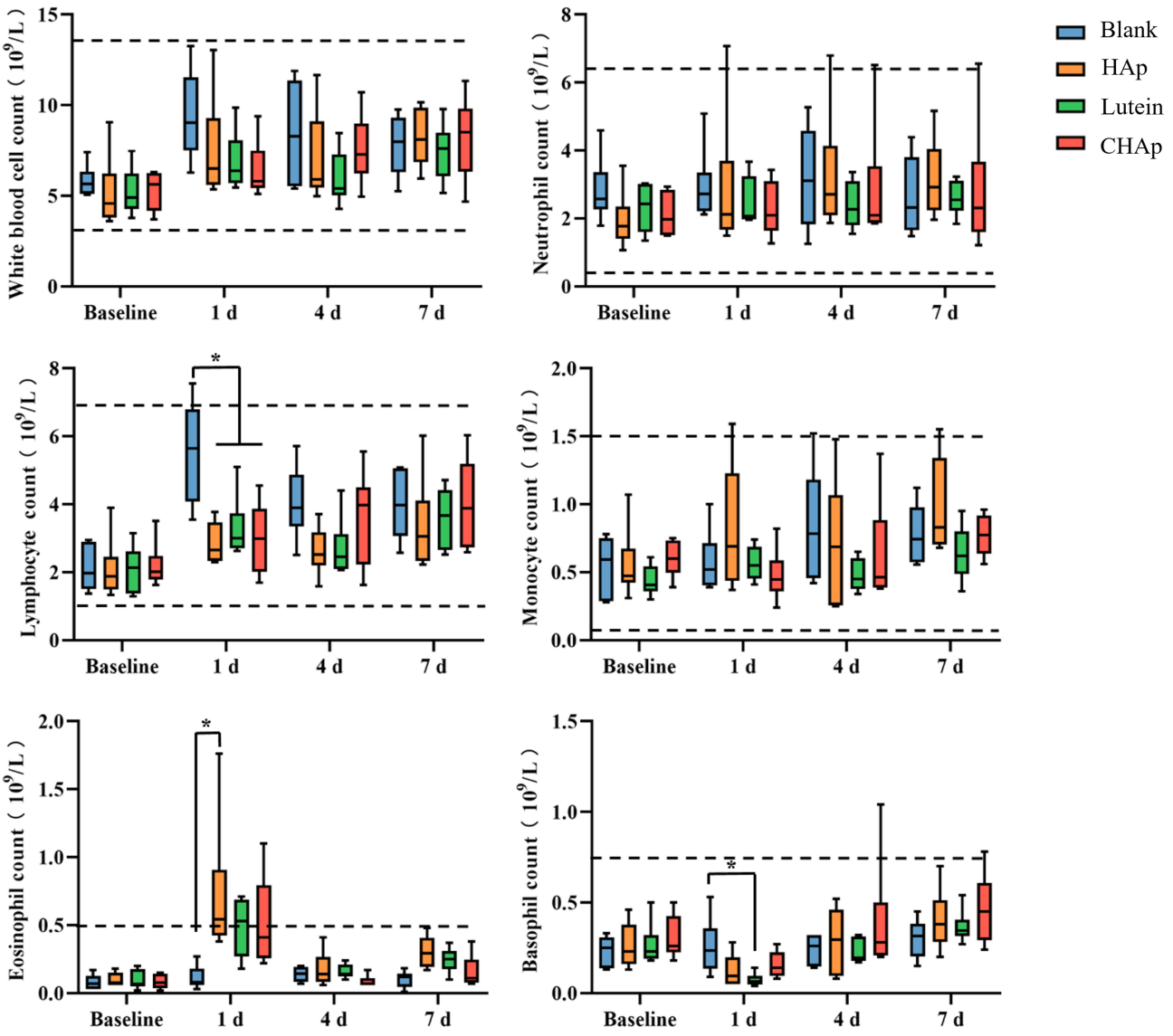

Figure 6 Blood routine was examined in the preoperative and postoperative venous blood of rabbits (n=6). The dotted line represents the normal reference values. *P* values were calculated along with comparisons between different groups (*P<0.05).

Discussion

HAp is a bone graft substitute with excellent osteoconductive and osteointegration properties.[39] Limited by the rate of degradation and mechanical properties, HAp is commonly applied as a coating on implants or in sites with low mechanical stress.[39,40] These drawbacks may partially be overcome by the development of 3D printing technology.

In this study, HAp and CHAp scaffolds were fabricated by 3D printing. SEM revealed dense pore channels on the surface of both scaffolds, which were formed by the vaporization of organic matter during the degreasing process. These pores could promote osteoblast adhesion and accelerate the rate of degradation in vivo. In addition, carbonate incorporation causes a decrease in the crystallinity of HAp,[41] which may be one of the reasons for the more loosely bound particles in the CHAp scaffold.

The scaffolds not only retain the excellent biocompatibility of hydroxylapatite-like materials but also provide a larger 3D space for cell growth. In vitro experiments, CHAp scaffolds showed improved cytocompatibility and osteoinductive properties, which might be attributed to its higher solubility.[34] Previous studies suggested that CHAp can form a microenvironment rich in Ca^{2+}, PO_4^{3-} and CO_3^{2-} on the surfaces, and these components were thought to assist the

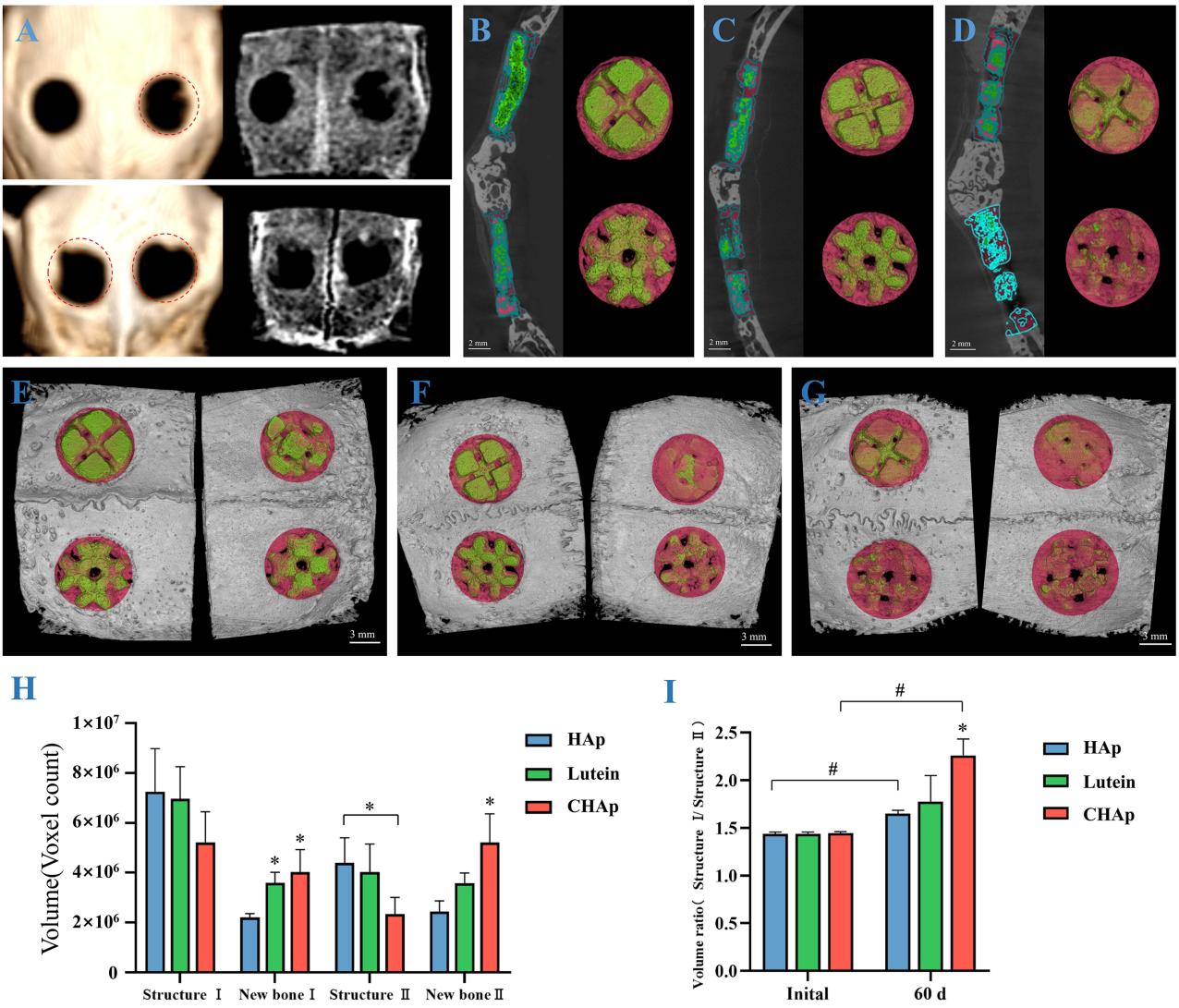

Figure 7 Radiographic imaging evaluation of bone defect repair (n=6). (**A**) Evaluation of skull defect repair without implant material, the red dashed box represents the initial 8 mm bone defect area. Micro-CT cross-sectional images and 3D reconstructions of bone defect sites in HAp group (**B**), lutein group (**C**), and CHAp group (**D**), green represents the implant material and red area represents new bone. 3D reconstruction of the skull in HAp group (**E**), lutein group (**F**), and CHAp group (**G**), with the external side of the skull on the left and the internal side of the skull on the right. (**H**) Residual scaffold volume and new bone volume within bone defects. (**I**) The volume ratio of S1 and S2 scaffolds. *P* values were calculated along with comparisons between different groups (*,#*P*<0.05).

osteogenesis process.[13,42,43] Besides, histological examination of calvarial defects further confirmed that bone cells can adhere and proliferate inside the 3D printed scaffolds via micro-pores.

The cellular experiments showed that lutein promoted differentiation and capacity of mineralization of osteoblasts. This is consistent with previous research that carotenoids can promote bone mineral deposition.[24,30] At bone defect site, exuberant cellular metabolism and inflammation often cause the production of excessive amounts of reactive oxygen species (ROS), which is detrimental to osteogenesis. Lutein carried on the scaffolds can scavenge ROS in time to protect bone tissue from oxidative stress and prevent ROS from triggering further inflammation.[44,45]

Evaluation of bone repair in the blank group showed that 8 mm diameter defects in the calvaria of rabbits did not heal properly, or was nonunion. In the scaffold implant groups, there was more new bone formation on the inner side of the skull. This might be attributed to the osteogenic cytokines produced by dura mater, such as transforming growth factor β1, fibroblast growth factor 2, and bone morphogenetic protein 2, which caused an increased rate and degree of osteoblast differentiation.[46,47] Micro-CT analysis of the CHAp scaffold showed a faster degradation and osteogenesis compared to the HAp scaffold. The faster degradation rate of CHAp provided osteocytes with a larger contact area and space, which

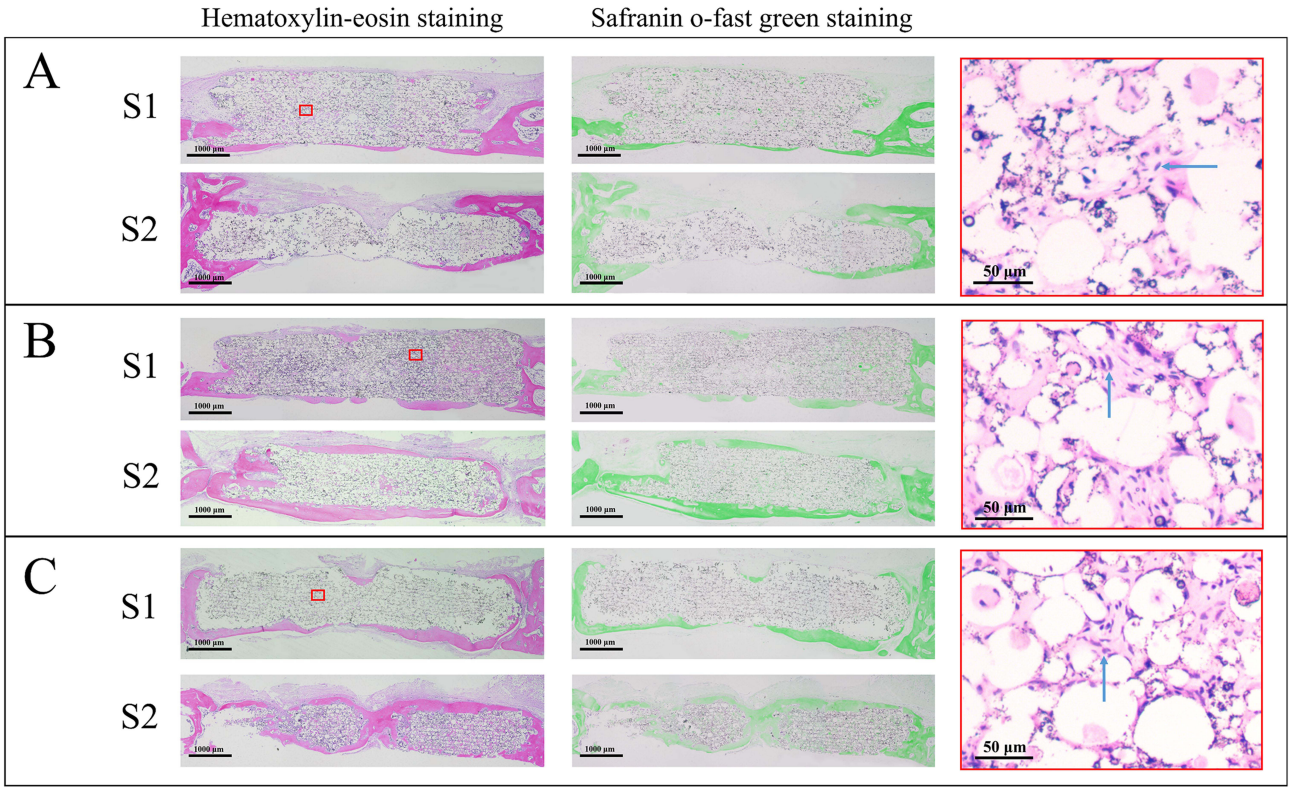

Figure 8 Histological sections of bone defect site in HAp group (**A**), lutein group (**B**), and CHAp group (**C**). Mineralized bone is stained in pink and green by Hematoxylin-eosin staining and Safranin O-fast green staining respectively. The red box shows the high-magnification imaging of the scaffold, and the blue arrow indicates bone cells.

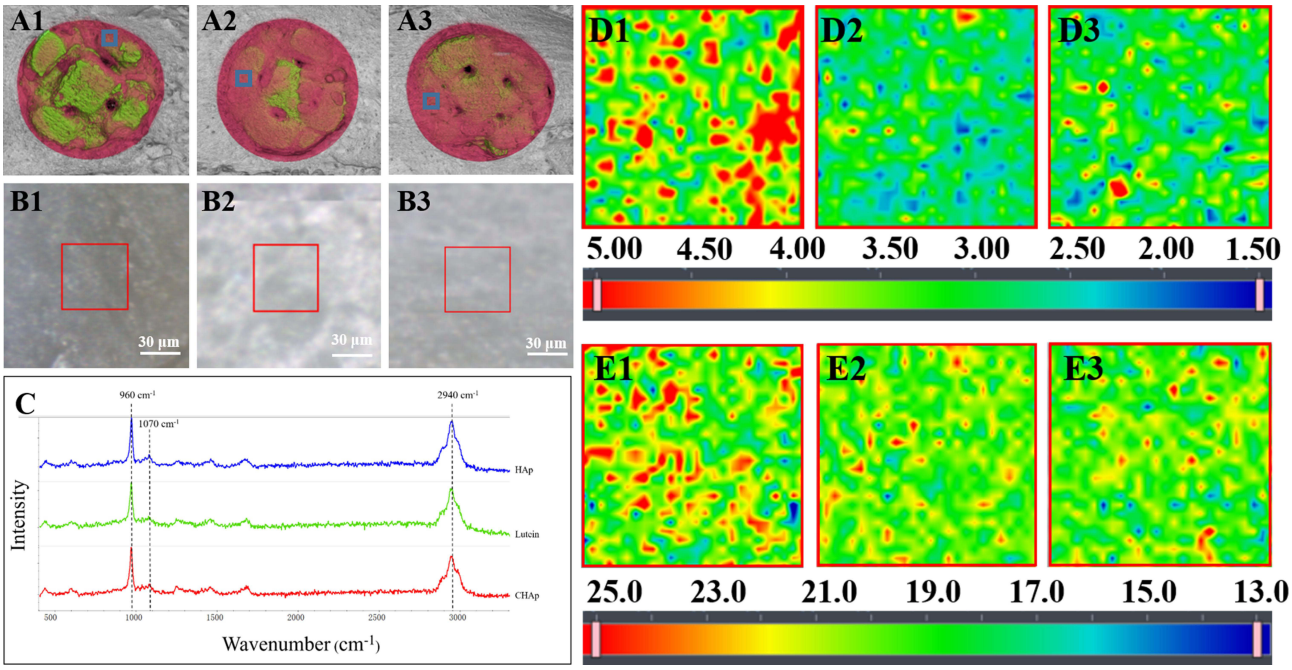

Figure 9 Raman mapping of new formation bone inside the bone defect. Raman mapping of new bone on scaffolds in HAp group (**A1**–**E1**), lutein group (**A2**–**E2**), and CHAp group (**A3**–**E3**), (**A**) is the internal side of the skull defect, blue boxes represent Raman detection area. (**B**) is the optical microscope image of the new bone, and the red box shows the Raman scan area. (**C**) is the Raman spectrum of the new bone. (**D**) represents the area ratio of the 2940 cm^{-1}/960 cm^{-1} peak, (**E**) represents the peak width at half height of the 960 cm^{-1} peak, and the corresponding values are represented by colors.

further promotes the function of osteocytes. Both S1 and S2 scaffolds have their own advantages. The S1 scaffold allows new bone to encapsulate the inner surface more quickly, providing better connection between the scaffold and the host bone. Ths S2 scaffold is able to be resorbed more quickly in vivo. In addition, the HAp scaffold combined with lutein can promote new bone formation but has no significant effect on the degradation rate of the scaffold. This may be attributed to the fact that lutein inhibits osteoclast activity,[48,49] whereas the degradation of apatite material requires the involvement of osteoclasts. Raman spectroscopy of new bone within the defect further demonstrated the ability of CHAp and lutein to promote bone mineralization.

Hematoma and acute inflammation typically occur within a week of a bone injury, and prolonged inflammation can lead to delayed healing or nonunion.[50–52] However, 3D printed scaffold implanted in rabbit skull did not cause a severe inflammatory response. The results of WBC showed that no serious infection occurred in the experimental rabbits within 7 days after the operation, indicating that the bone repair in the later period was not affected by persistent inflammation. Furthermore, the rabbits in the blank group had higher levels of WBC at 1–4 d postoperatively than the other groups, which suggested that the HAp material would not stimulate the body to produce an inflammatory response, but rather controls the development of inflammation by inhibiting hematoma formation due to the filling effect.

The CHAp scaffolds synthesized in this study have a faster in-vivo degradation rate compared to normal HAp scaffolds and also promote osteogenesis at the bone defect site. This study is a preliminary attempt to apply CHAp in the treatment of bone defects and does not investigate the properties of CHAp composites. Future studies will focus on the composite of CHAp with other biomaterials for more clinically valuable products.

Conclusion

3D printed scaffolds designed in this study provide a larger contact area for cell adhesion, and new formation bone can grow deeper into the scaffolds along with the reserved pores, greatly accelerating the rate of degradation. The incorporation of suitable carbonates into HAp can accelerate the degradation of the materials and the formation of new bone, while the incorporation of lutein into graft materials can also promote bone formation, all of which provide a new reference for the research and application of apatite-based composites. Future studies will focus on the composite of CHAp with other biomaterials for better clinical efficacy.

Acknowledgments

This work was supported by the National Natural Science Foundation of China (No. 32072936). The work was also partially funded by State Key Laboratory of Palaeobiology and Stratigraphy (Nanjing Institute of Geology and Palaeontology, CAS (No. 223116)).

Disclosure

The authors report no conflicts of interest in this work.

References

1. Reichert JC, Saifzadeh S, Wullschleger ME, et al. The challenge of establishing preclinical models for segmental bone defect research. *Biomaterials*. 2009;30(12):2149–2163. doi:10.1016/j.biomaterials.2008.12.050
2. Wang W, Yeung K. Bone grafts and biomaterials substitutes for bone defect repair: a review. *Bioact Mater*. 2017;2(4):224–247. doi:10.1016/j.bioactmat.2017.05.007
3. Van der Stok J, Van Lieshout EM, El-Massoudi Y, Van Kralingen GH, Patka P. Bone substitutes in the Netherlands–a systematic literature review. *Acta Biomater*. 2011;7(2):739–750. doi:10.1016/j.actbio.2010.07.035
4. Bauer TW, Muschler GF. Bone graft materials: an overview of the basic science. *Clin Orthopaedics Related Res*. 2000;371:37110–37127.
5. Fernandez-Yague MA, Abbah SA, McNamara L, Zeugolis DI, Pandit A, Biggs MJ. Biomimetic approaches in bone tissue engineering: integrating biological and physicomechanical strategies. *Adv Drug Delivery Rev*. 2015;84:1–29.
6. Zimmermann G, Moghaddam A. Allograft bone matrix versus synthetic bone graft substitutes. *Injury*. 2011;42:42S16–42S21.
7. Khan SN, Cammisa FP, Sandhu HS, Diwan AD, Girardi FP, Lane JM. The biology of bone grafting. *J Am Acad Orthop Surg*. 2005;13(1):77–86. doi:10.5435/00124635-200501000-00010
8. Finkemeier CG. Bone-grafting and bone-graft substitutes. *JBJS*. 2002;84(3):454–464. doi:10.2106/00004623-200203000-00020
9. Lee EJ, Kasper FK, Mikos AG. Biomaterials for tissue engineering. *Ann Biomed Eng*. 2014;42(2):323–337. doi:10.1007/s10439-013-0859-6
10. Asselmeier MA, Caspari RB, Bottenfield S. A review of allograft processing and sterilization techniques and their role in transmission of the human immunodeficiency virus. *Am j Sports Med*. 1993;21(2):170–175. doi:10.1177/036354659302100202

11. Archunan MW, Petronis S. Bone grafts in trauma and orthopaedics. *Cureus*. 2021;13(9).
12. Barradas A, Yuan H, van Blitterswijk CA, Habibovic P. Osteoinductive biomaterials: current knowledge of properties, experimental models and biological mechanisms. *Eur Cell Mater*. 2011;21(407):29. doi:10.22203/eCM.v021a31
13. Samavedi S, Whittington AR, Goldstein AS. Calcium phosphate ceramics in bone tissue engineering: a review of properties and their influence on cell behavior. *Acta Biomater*. 2013;9(9):8037–8045. doi:10.1016/j.actbio.2013.06.014
14. Klinge B, Alberius P, Isaksson S, Jönsson J. Osseous response to implanted natural bone mineral and synthetic hydroxylapatite ceramic in the repair of experimental skull bone defects. *J Oral Maxillofacial Surg*. 1992;50(3):241–249. doi:10.1016/0278-2391(92)90320-Y
15. Jarcho M, Kay JF, Gumaer KI, Doremus RH, Drobeck HP. Tissue, cellular and subcellular events at a bone-ceramic hydroxylapatite interface. *J Bioeng*. 1977;1(2):79–92.
16. Heimann RB. Functional plasma-sprayed hydroxylapatite coatings for medical application: clinical performance requirements and key property enhancement. *J Vac Sci Technol A*. 2021;39(5):050801. doi:10.1116/6.0001132
17. Eggli P, Müller W, Schenk R. Porous hydroxyapatite and tricalcium phosphate cylinders with two different pore size ranges implanted in the cancellous bone of rabbits. A comparative histomorphometric and histologic study of bony ingrowth and implant substitution. *Clin Orthopaedics Related Res*. 1988;232:127–138.
18. Cahyanto A, Maruta M, Tsuru K, Matsuya S, Ishikawa K. Fabrication of bone cement that fully transforms to carbonate apatite. *Dent Mater J*. 2015;34(3):2014–2328.
19. Amna T. Valorization of bone waste of Saudi Arabia by synthesizing hydroxyapatite. *Appl Biochem Biotechnol*. 2018;186(3):779–788. doi:10.1007/s12010-018-2768-5
20. Rahyussalim AJ, Supriadi S, Marsetio AF, Pribadi PM, Suharno B. The potential of carbonate apatite as an alternative bone substitute material. *Med J Indonesia*. 2019;28(1):92–97. doi:10.13181/mji.v28i1.2681
21. Chissov V, Sviridova I, Sergeeva N, et al. Study of in vivo biocompatibility and dynamics of replacement of rat shin defect with porous granulated bioceramic materials. *Bull Exp Biol Med*. 2008;146(1):139–143. doi:10.1007/s10517-008-0222-3
22. Hing K, Annaz B, Saeed S, Revell P, Buckland T. Microporosity enhances bioactivity of synthetic bone graft substitutes. *J Mater Sci*. 2005;16(5):467–475. doi:10.1007/s10856-005-6988-1
23. Bignon A, Chouteau J, Chevalier J, et al. Effect of micro-and macroporosity of bone substitutes on their mechanical properties and cellular response. *J Mater Sci*. 2003;14(12):1089–1097. doi:10.1023/b:jmsm.0000004006.90399.b4
24. Zia-Ul-Haq M, Riaz M, Modhi AO. Carotenoids and bone health. In: *Carotenoids: Structure and Function in the Human Body*. Springer; 2021:697–713.
25. Rao AV, Rao LG. Carotenoids and human health. *Pharmacol Res*. 2007;55(3):207–216. doi:10.1016/j.phrs.2007.01.012
26. Dai Z, Wang R, Ang LW, Low YL, Yuan JM, Koh WP. Protective effects of dietary carotenoids on risk of hip fracture in men: the Singapore Chinese Health Study. *J Bone Miner Res*. 2014;29(2):408–417. doi:10.1002/jbmr.2041
27. Xu J, Song C, Song X, Zhang X, Li X. Carotenoids and risk of fracture: a meta-analysis of observational studies. *Oncotarget*. 2017;8(2):2391. doi:10.18632/oncotarget.13678
28. Uchiyama S, Yamaguchi M. Oral administration of β-cryptoxanthin prevents bone loss in ovariectomized rats. *Int J Mol Med*. 2006;17(1):15–20.
29. Fuad NIN, Sekar M, Gan SH, Lum PT, Vaijanathappa J, Ravi SL. A comprehensive review on its chemical, biological activities and therapeutic potentials; 2020.
30. Tominari T, Matsumoto C, Watanabe K, et al. Lutein, a carotenoid, suppresses osteoclastic bone resorption and stimulates bone formation in cultures. *Biosci Biotechnol Biochem*. 2017;81(2):302–306. doi:10.1080/09168451.2016.1243983
31. Kim L, Rao AV, Rao LG. Lycopene II—effect on osteoblasts: the carotenoid lycopene stimulates cell proliferation and alkaline phosphatase activity of SaOS-2 cells. *J Med Food*. 2003;6(2):79–86. doi:10.1089/109662003322233468
32. Oliveira GR, Vargas-Sanchez PK, Fernandes RR, et al. Lycopene influences osteoblast functional activity and prevents femur bone loss in female rats submitted to an experimental model of osteoporosis. *J Bone Mineral Metabol*. 2019;37(4):658–667. doi:10.1007/s00774-018-0970-8
33. Ermakov IV, Ermakova MR, Rosenberg TD, Gellermann W. Optical detection of carotenoid antioxidants in human bone and surrounding tissue. *J Biomed Opt*. 2013;18(11):117006. doi:10.1117/1.JBO.18.11.117006
34. Wang S, Zhang J, Ma J, et al. Applying Pb2+ to probe the dissolution of carbonated hydroxylapatite by enterobacter sp.: a new insight into the bioerosion of tooth mineral. *J Biomed Mater Res Part B*. 2021;109(8):1230–1238. doi:10.1002/jbm.b.34784
35. Liu Z, Liang H, Shi T, et al. Additive manufacturing of hydroxyapatite bone scaffolds via digital light processing and in vitro compatibility. *Ceram Int*. 2019;45(8):11079–11086. doi:10.1016/j.ceramint.2019.02.195
36. Cao Y, Shi T, Jiao C, et al. Fabrication and properties of zirconia/hydroxyapatite composite scaffold based on digital light processing. *Ceram Int*. 2020;46(2):2300–2308. doi:10.1016/j.ceramint.2019.09.219
37. Antonakos A, Liarokapis E, Leventouri T. Micro-Raman and FTIR studies of synthetic and natural apatites. *Biomaterials*. 2007;28(19):3043–3054. doi:10.1016/j.biomaterials.2007.02.028
38. Fleet ME. Infrared spectra of carbonate apatites: ν2-Region bands. *Biomaterials*. 2009;30(8):1473–1481. doi:10.1016/j.biomaterials.2008.12.007
39. Bhatt RA, Rozental TD. Bone graft substitutes. *Hand Clinics*. 2012;28(4):457–468. doi:10.1016/j.hcl.2012.08.001
40. Roberts TT, Rosenbaum AJ. Bone grafts, bone substitutes and orthobiologics: the bridge between basic science and clinical advancements in fracture healing. *Organogenesis*. 2012;8(4):114–124. doi:10.4161/org.23306
41. Wang S, Zhang P, Kong X, et al. Delicate changes of bioapatite mineral in pig femur with addition of dietary xylooligosaccharide: evidences from Raman spectroscopy and ICP. *Anim Sci J*. 2017;88(11):1820–1826.
42. Lin K, Wu C, Chang J. Advances in synthesis of calcium phosphate crystals with controlled size and shape. *Acta Biomater*. 2014;10(10):4071–4102. doi:10.1016/j.actbio.2014.06.017
43. Best S, Porter A, Thian E, Huang J. Bioceramics: past, present and for the future. *J Eur Ceram Soc*. 2008;28(7):1319–1327. doi:10.1016/j.jeurceramsoc.2007.12.001
44. Reuter S, Gupta SC, Chaturvedi MM, Aggarwal BB. Oxidative stress, inflammation, and cancer: how are they linked? *Free Radic Biol Med*. 2010;49(11):1603–1616. doi:10.1016/j.freeradbiomed.2010.09.006
45. Chatterjee S. Oxidative stress, inflammation, and disease. In: *Oxidative Stress and Biomaterials*. Elsevier; 2016:35–58.

46. Spector JA, Greenwald JA, Warren SM, et al. Co-culture of osteoblasts with immature dural cells causes an increased rate and degree of osteoblast differentiation. *Plast Reconst Surg*. 2002;109(2):631–642, discussion 643. doi:10.1097/00006534-200202000-00033
47. Levi B, Nelson ER, Li S, et al. Dura mater stimulates human adipose-derived stromal cells to undergo bone formation in mouse calvarial defects. *Stem Cells*. 2011;29(8):1241–1255. doi:10.1002/stem.670
48. Yamaguchi M. β-Cryptoxanthin and bone metabolism: the preventive role in osteoporosis. *J Health Sci*. 2008;54(4):356–369. doi:10.1248/jhs.54.356
49. Yamaguchi M, Uchiyama S. β-Criptoxanthin stimulates bone formation and inhibits bone resorption in tissue culture in vitro. *Mol Cell Biochem*. 2004;258(1):137–144. doi:10.1023/B:MCBI.0000012848.50541.19
50. Claes L, Recknagel S, Ignatius A. Fracture healing under healthy and inflammatory conditions. *Nat Rev Rheumatol*. 2012;8(3):133–143. doi:10.1038/nrrheum.2012.1
51. Marsell R, Einhorn TA. The biology of fracture healing. *Injury*. 2011;42(6):551–555. doi:10.1016/j.injury.2011.03.031
52. Kolar P, Schmidt-Bleek K, Schell H, et al. The early fracture hematoma and its potential role in fracture healing. *Tissue Eng B*. 2010;16(4):427–434. doi:10.1089/ten.teb.2009.0687